Phonon-mediated superconductivity in magic-strain bilayer graphene

Qingxiang Ji,[1,*] Bohan Li,[1,*] Johan Christensen,[2] Changguo Wang,[1,†] and Muamer Kadic[3,‡]
[1]*National Key Laboratory of Science and Technology on Advanced Composites in Special Environments, Harbin Institute of Technology, Harbin 150001, People's Republic of China*
[2]*IMDEA Materials Institute, Calle Eric Kandel 2, 28906 Getafe (Madrid), Spain*
[3]*Université Marie et Louis Pasteur, Institut FEMTO-ST, CNRS, 25000 Besançon, France*

(Received 14 September 2024; revised 6 June 2025; accepted 22 July 2025; published 4 August 2025)

Extensive investigations on the moiré magic angle have been conducted in twisted bilayer graphene, unlocking the mystery of unconventional superconductivity and insulating states. In analogy to the magic angle, here we demonstrate the concept of magic strain in graphene systems by judiciously tailoring mechanical relaxation (stretch and compression) which is easier to implement in practice. We elucidate the interplay of strain-induced effects and delve into the resulting unconventional superconductivity or semimetal-insulator transition in relaxation-strained graphene, going beyond the traditional twisting approach. Our findings reveal how relaxation strain can trigger superconducting transitions (with an ultraflat band at the Fermi level) or a semimetal-insulator transition (with a gap opening at the K point of 0.39 eV) in both monolayer and bilayer graphene. These discoveries open up another branch for correlated phenomena and provide deeper insights into the underlying physics of superconductors, which positions graphene as a highly tunable platform for different electronic applications.

DOI: 10.1103/5v5w-8vtn

I. INTRODUCTION

Functional materials are engineered materials designed with specific functionalities in mind. They play a crucial role in various technological advancements to harness sound [1–3], light [4], vibrations [5], heat [6,7], and electronic states [8,9]. For many years, classical metamaterials have been the workhorse of the functional materials field. By manipulating their artificial structure features at the subwavelength scale, metamaterials achieve an array of exotic properties not found in natural materials [10]. For instance, metamaterials can bend light or sound in unusual ways, create invisibility cloaks, or possess a negative refractive index [11,12].

In recent years, a new class of functional materials has emerged, called van der Waals (vdW) metamaterials. As the name suggests, vdW metamaterials are the marriage of vdW materials and metamaterial design principles. They create intricate heterostructures by stacking different vdW materials. These heterostructures can be tailored to exhibit entirely new properties due to the combined effects of their individual components [13–15], opening doors to novel functionalities not achievable by classical metamaterials alone. The vdW metamaterials have shown great potential as tunable correlated electron systems, and have demonstrated various intriguing properties by varying the stacking configuration of low-dimensional material sheets, e.g., graphene and MXenes [16–20]. For graphene, the emergent heterostructures have added to them a long list of miraculous properties such as the superconducting and insulating state. Compared to other superconducting materials with intense doping [21], e.g., copper oxide [22], iron-based [23], and MgB_2 superconductors [24], graphene has unique advantages of being a single-atomic lattice structure. This superlattice characteristic expands the possibilities to tune graphene's conductivity properties by tailoring its heterostructure using mechanical deformation/strain. Strain is an effective way for engineering flat bands that favor the emergence of superconductivity or other correlated phases [25–33]. Recently, experiments have demonstrated superconducting states in twisted bilayer graphene (TBG) [34]. The superconductivity of twisted graphene systems is rooted in the moiré modulation of the interlayer coupling, which is depicted by Dirac models that flatten the electronic bands at particular angles [35,36]. The fascinating physics of correlated graphene moiré superlattices, such as TBG, has generated extensive efforts to uncover the mysteries of their phase diagrams [37]. As a typical example, independent-layer behavior and the reduction of the Fermi velocity are observed for small angles in TBG. Specifically, when the torsional angle is close to 1.1° (magic angle), superconductivity and Mott insulator behavior can be induced in TBG. In addition, magic angles can also cause some exotic phenomena in optics and mechanics [38,39]. So far, there has been an explosion of research conducted on twisting modulation. However, accurate twisting is laborious and needs intense efforts during sample fabrication. The influence of in-plane stain/deformation generated during the twisting process is also neglected [40–42].

Compared with twisting, relaxation (stretch or compression), which is widely adopted in mechanics, is easier to implement and holds the potential for large-scale device applications. Researchers demonstrate that modulating relaxation

*These authors contributed equally to this work.
†Contact author: wangcg@hit.edu.cn
‡Contact author: muamer.kadic@femto-st.fr

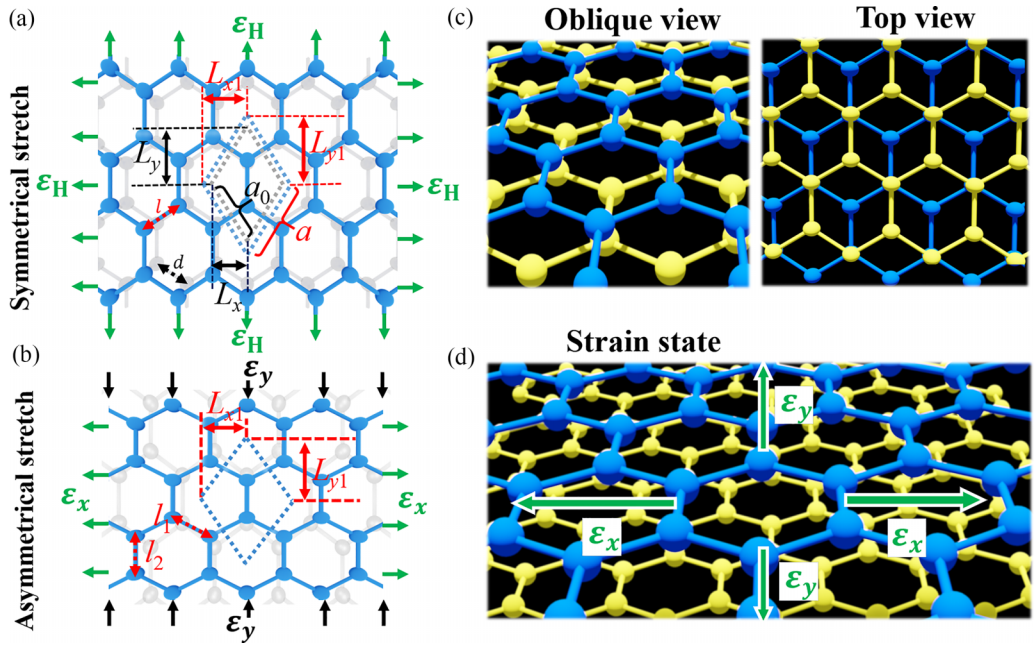

FIG. 1. Relaxation strain of monolayer graphene with (a) symmetrical deformation ($\varepsilon_x = \varepsilon_y = \varepsilon_H$) and (b) asymmetrical deformation along the x and y directions ($\varepsilon_x \neq \varepsilon_y$). Here, the graphene in white (blue) is pristine (deformed), and L_x (L_{x_1}) and L_y (L_{y_1}) are the half diagonal lengths of the pristine (deformed) cells, respectively. Diagrams of (c) pristine and (d) deformed bilayer graphene are also depicted.

strain can generate an approximate flat-band state or induce a band gap in monolayer graphene, similar to those produced in twisted bilayer configurations. Experiments that engineer relaxation strain on graphene membranes have reported unexpected electronic transport and peculiar features of the local density of states [43,44]. Although intriguing phenomena have been predicted, there is a gap in connecting the unconventional properties to distinct strain behavior. Knowledge of the strain features that determine the resulting electronic properties is highly desirable. Currently various strain conditions have been implemented in monolayer graphene, but the band-gap tunability is relatively confined. For bilayer graphene, the strain effects are studied all within the framework of twisted conditions [45–47]. We note that using biaxial relaxation strain on graphene systems (monolayer and bilayer) to achieve unconventional properties, which is predicted to have a higher degree of tunability (meanwhile being more complicated), remains elusive. Consequently, the potential of relaxation-strained graphene to tailor electronic properties remains untapped.

In this work, we address these issues by developing tight-binding models that control biaxial strain on graphene sheets. First, we study monolayer graphene with a symmetrical strain distribution and demonstrate that relaxation will influence the Fermi velocity near the K point. Based on this finding, we adopt a general deformation manner where the graphene is stretched in one direction and compressed in the perpendicular direction. This technique allows us to open the band gap widely (0.39 eV) and generate a semimetal-insulator transition for monolayer graphene. Then we turn to investigate Bernal-stacked graphene and reveal the relationship between interlayer distance and weak van der Waals force for bilayer graphene systems. By fixing one graphene layer and stretching another layer with a symmetrical strain rate of 1.9% (magic strain), we display unambiguously a flat band at the Fermi level, indicating a superconducting transition. In addition, the asymmetric strain on bilayer graphene will open the band gap with small margins (0.0272 eV), much less than the monolayer counterpart (0.39 eV).

II. MATERIAL AND METHODS

We construct a tight-binding model (TBM) for monolayer graphene sheets, based on which we investigate the band structure considering two types of strain distributions:

(i) Symmetrical strain distribution which retains hexagonal symmetry and is defined as $\varepsilon_H = (a - a_0)/a_0$: The terms a and a_0 denote the lattice parameters before and after deformation, respectively [Fig. 1(a)].

(ii) Asymmetrical strain distribution along the x (or y) direction which corresponds to strain parallel to the zigzag (or armchair) edge of graphene ribbons and is defined as $\varepsilon_x = (L_{x1} - L_x)/L_x$ [or $\varepsilon_y = (L_{y1} - L_y)/L_y$] and $\varepsilon_x \neq \varepsilon_y$: Here, L_x (L_{x1}) and L_y (L_{y1}) are the half diagonal lengths of the pristine (deformed) cells [Fig. 1(b)].

We first establish the TBM for symmetrical strained monolayer graphene only considering on-site and nearest-neighbor hopping, as shown in Fig. 1(a). The Hamiltonian for monolayer graphene can be expressed as

$$H = -t \sum_{\boldsymbol{R}} c_A^\dagger(\boldsymbol{R})[c_A(\boldsymbol{R}) + c_B(\boldsymbol{R} - \boldsymbol{a}_1) + c_B(\boldsymbol{R} - \boldsymbol{a}_2)] + \text{H.c.}, \tag{1}$$

where $c_A^\dagger(\boldsymbol{R})$ and $c_A(\boldsymbol{R})$ are creation (annihilation) operators for an electron in an atomiclike state of kind A (i.e., three adjacent carbon atoms form a regular triangle). The terms $\boldsymbol{a}_1$ and $\boldsymbol{a}_2$ are basis vectors for the unit cell, $\boldsymbol{R}$ is the position of the unit cell, and H.c. stands for the Hermitian conjugate. We obtain the Hamiltonian for symmetrical strained monolayer graphene $H_{\mathrm{SMG}}(\boldsymbol{k})$ by

$$H_{\mathrm{SMG}}(\boldsymbol{k}) = \begin{bmatrix} 0 & -tf(\boldsymbol{k}) \\ -tf^*(\boldsymbol{k}) & 0 \end{bmatrix}, \tag{2}$$

where we have $f(\boldsymbol{k}) = \sum_{i=1}^{3} e^{i\boldsymbol{k}\cdot\boldsymbol{d}_i}$ and $\boldsymbol{d}_1 = (\boldsymbol{a}_1 + \boldsymbol{a}_2)(1 + \varepsilon_{\mathrm{H}})/3$, $\boldsymbol{d}_2 = (-2\boldsymbol{a}_1 + \boldsymbol{a}_2)(1 + \varepsilon_{\mathrm{H}})/3$, $\boldsymbol{d}_3 = (\boldsymbol{a}_1 - 2\boldsymbol{a}_2)(1 + \varepsilon_{\mathrm{H}})/3$. After imposing symmetrical strain distributions, the hopping parameters t with the bond length are expressed as $V_{pp\pi}(l) = t_0 e^{-3.37(l/d-1)}$, where d is the carbon-carbon bond length for undeformed graphene [48,49].

For asymmetrical strained monolayer graphene [Fig. 1(b)], the Hamiltonian changes its form to

$$H_{\mathrm{ASMG}}(\boldsymbol{k}) = \begin{bmatrix} 0 & -(t_2 - t_1) - t_1 f(\boldsymbol{k}) \\ (-t_2 - t_1) - t_1 f^*(\boldsymbol{k}) & 0 \end{bmatrix}, \tag{3}$$

where the new added terms $t_1 = V_{pp\pi}(l_1)$ and $t_2 = V_{pp\pi}(l_2)$ denote the hopping parameters.

We then move to construct TBM of bilayer graphene considering only a homogeneous interlayer hopping between the nearest neighbors, as shown in Fig. 1(c). The Hamiltonian can be written as the sum of the following terms,

$$H = H_1 + H_2 + \langle 1, \boldsymbol{R}, A|H_\perp|2, \boldsymbol{R}, B\rangle \sum_{\boldsymbol{R}} c_{1,A}^\dagger(\boldsymbol{R}) c_{2,B}(\boldsymbol{R}) + \mathrm{H.c.}, \tag{4}$$

where H_1 and H_2 are the Hamiltonian for each monolayer graphene, while $H_\perp$ indicates Hamiltonian interlayer coupling in the second quantized formalism. The Hamiltonian $H_{\mathrm{BLG}}(\boldsymbol{k})$ of Bernal-stacked bilayer graphene is

$$H_{\mathrm{BLG}}(\boldsymbol{k}) = \begin{bmatrix} 0 & -tf(\boldsymbol{k}) & 0 & \langle 1, \boldsymbol{R}, A|H_\perp|2, \boldsymbol{R}, B\rangle \\ -tf^*(\boldsymbol{k}) & 0 & 0 & 0 \\ 0 & 0 & 0 & -tf(\boldsymbol{k}) \\ \langle 1, \boldsymbol{R}, A|H_\perp|2, \boldsymbol{R}, B\rangle & 0 & -tf^*(\boldsymbol{k}) & 0 \end{bmatrix}. \tag{5}$$

For bilayer graphene systems with biaxial deformation [shown in Fig. 1(d)], we construct a low-energy continuum model that consists of three terms: two single-layer Dirac-Hamiltonian terms that account for the isolated graphene sheets, and a tunneling term that describes hopping between the two layers. Considering only the K points of the three closest neighbors, we can get Hamiltonian $H_{\mathrm{SBLG}}(\boldsymbol{k})$ for bilayer-strained graphene as

$$H_{\mathrm{SBLG}}(\boldsymbol{k}) = \begin{bmatrix} H_{\mathrm{MG}}^{\boldsymbol{k}}\left(\frac{\varepsilon_x}{2}, \frac{\varepsilon_y}{2}\right) & T_{\boldsymbol{q}_b} & T_{\boldsymbol{q}_{tr}} & T_{\boldsymbol{q}_{tl}} \\ T_{\boldsymbol{q}_b}^\dagger & H_{\mathrm{MG}}^{\boldsymbol{k}_b}\left(-\frac{\varepsilon_x}{2}, -\frac{\varepsilon_y}{2}\right) & 0 & 0 \\ T_{\boldsymbol{q}_{tr}}^\dagger & 0 & H_{\mathrm{MG}}^{\boldsymbol{k}_{tr}}\left(-\frac{\varepsilon_x}{2}, -\frac{\varepsilon_y}{2}\right) & 0 \\ T_{\boldsymbol{q}_{tl}}^\dagger & 0 & 0 & H_{\mathrm{MG}}^{\boldsymbol{k}_{tl}}\left(-\frac{\varepsilon_x}{2}, -\frac{\varepsilon_x}{2}\right) \end{bmatrix}. \tag{6}$$

Here, H_{MG} is the Hamiltonian for monolayer graphene, i.e., $H_{\mathrm{SMG}}(\boldsymbol{k})$ for a symmetrical and $H_{\mathrm{ASMG}}(\boldsymbol{k})$ for an asymmetrical system, and T is the tunneling term for interlayer hopping. On the basis of the Hamiltonian matrix, we further obtain the renormalization of Fermi velocity v_{F}^*,

$$\frac{v_{\mathrm{F}}^*(\theta)}{v_{\mathrm{F}}} = 1 - \left(\frac{t_\perp(K)}{v_{\mathrm{F}}\hbar|\boldsymbol{k}|A_{\mathrm{u.c.}}}\right)^2 \frac{1}{\sqrt{\left(\varepsilon_x^2 + \varepsilon_y^2\right)/2}}, \tag{7}$$

where $A_{\mathrm{u.c.}}$ is the unit cell area, $t_\perp(K) = 0.58$ eV Å^2 denotes the interlayer hopping term for Bernal stacked bilayer graphene, V_{F} is the pristine Fermi velocity, and $\hbar$ is the Planck constant. Following Eq. (7), Fermi velocity will decay to zero under small ε_x and ε_y, which potentially generates superconductivity. Details of the TBM are presented in the Supplemental Material [50] (see also Refs. [51,52] therein).

III. RESULTS AND DISCUSSION

A. Semimetal-insulator transition in monolayer graphene

To verify the accuracy of the established TBM, we conduct simulations based on first-principles calculations of density functional theory (DFT). The results by TBM and DFT simulations show perfect agreement with each other, as shown in Fig. 2. In the symmetrical strain conditions ($\epsilon_x = \epsilon_y \neq 0$), we observe that the slope of the band structure decreases near the K point, which indicates the decrement of Fermi velocity according to the law $V_{\mathrm{F}} = 2\pi E/(\hbar k)$. In addition, the band gap is observed to be zero, because the symmetrical strain field retains the geometrical symmetry of hexagonal lattices. In the asymmetrical strain conditions ($\epsilon_x \neq \epsilon_y \neq 0$), the band gap will open near the K and R high-symmetry points, due to the destruction of geometrical symmetry in hexagonal lattices, as observed in Figs. 2(e) and 2(f). Such a band-gap-opening phenomenon indicates that monolayer graphene generates semimetal-insulator transitions. The partial enlargement of these band structures is presented as insets

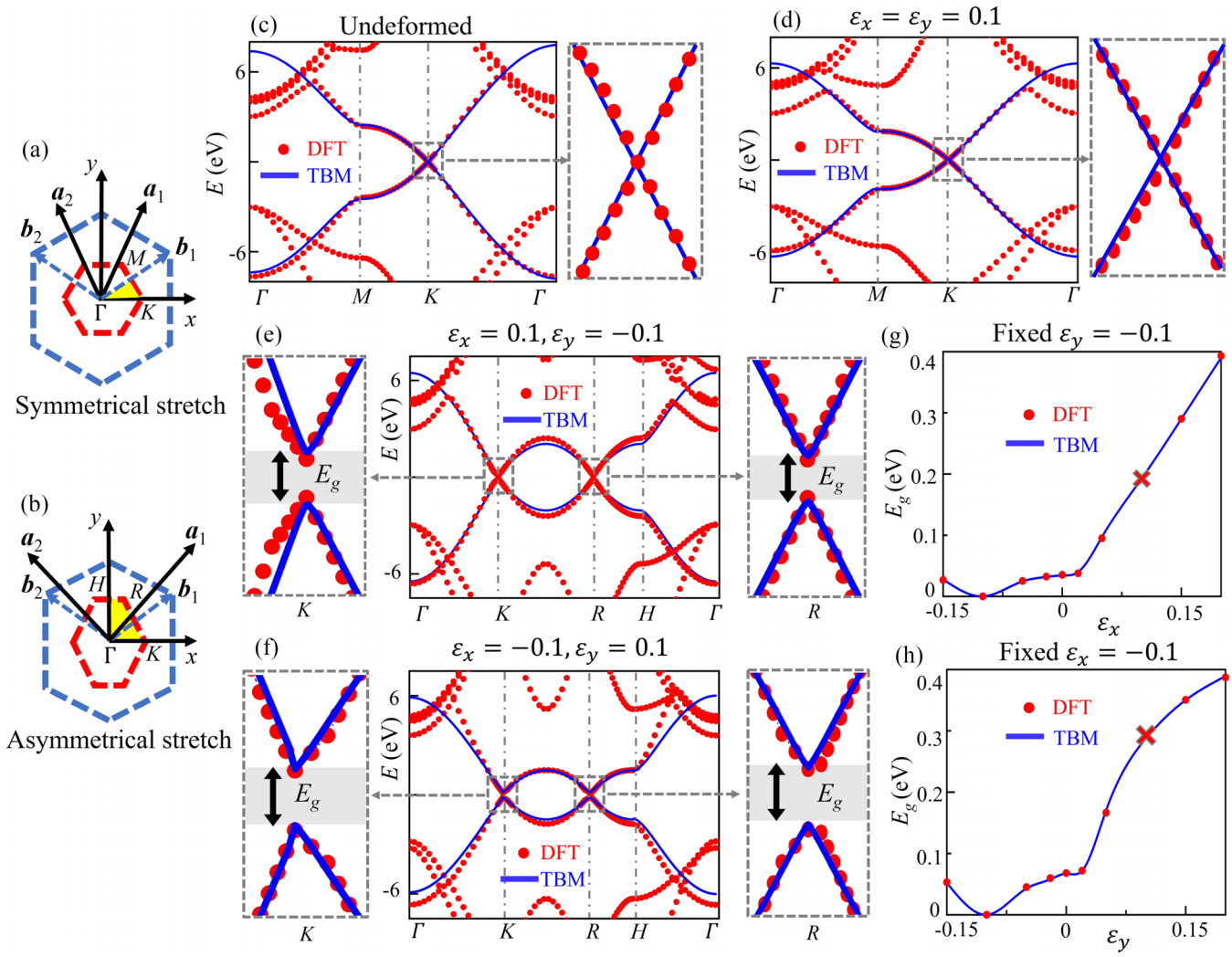

FIG. 2. Semimetal-insulator transition for monolayer graphene. Irreducible Brillouin zones (in yellow) are shown for monolayer graphene under (a) symmetrical and (b) asymmetrical stretching. Reciprocal lattices (in navy dashed lines) and Brillouin zones (in red dashed lines) are depicted for clarity. Band structures of monolayer graphene are obtained by TBM (by blue solid lines) and DFT (by red dots) methods considering (c) pristine, (d) symmetrical strain, and (e), (f) asymmetrical strain, respectively. The zooms show that band gaps E_g are generated only in asymmetrical strain cases around the K point and R point, indicating semimetal-insulator transitions. (g), (h) Such band gaps are further plotted as a function of ε_x and ε_y, where we use a cross to mark the strain conditions corresponding to (e) and (f).

in Figs. 2(g) and 2(h) which depicts the general relationship between the band gap and the strain. Results show that the band gap will open wodely if monolayer graphene is stretched in one direction while compressed in another direction, i.e., inhomogeneous strain condition $\epsilon_x\epsilon_y < 0$. It is also found that the band-gap value increases with an increase of applied strain differences. We get a band gap of 0.39 eV when the strain condition $\epsilon_x = -10\%$, $\epsilon_y = 20\%$ is imposed. This value is much larger than unidirectional stretch or compression obtained in the literature [48]. In addition, by releasing homogeneous strain in orthogonal directions (compressive strain only or tensile strain only, $\epsilon_x\epsilon_y > 0$), we can still obtain a band-gap opening, but smaller than the inhomogeneous strain conditions. This can be intuitively interpreted from the fact that inhomogeneous strain conditions will result in a larger destruction of the geometrical symmetry in hexagonal lattices.

B. Phonon-mediated superconductivity in bilayer graphene

We then investigate the band structures of Bernal-stacked bilayer graphene. The influence of interlayer distance is first studied based on TBM and DFT methods. Results in Figs. 3(a) and 3(b) show that the valence band and conduction band will get separated respectively when the interlayer distance is $h = 5$ Å. Such a phenomenon is induced by the weak van der Waals force [53], and this result agrees well with the literature [49]. We further reveal the dependence of such separation E_p on the interlayer distance in Fig. 3(c), where E_p is the separation value of the conduction band at the K point. With

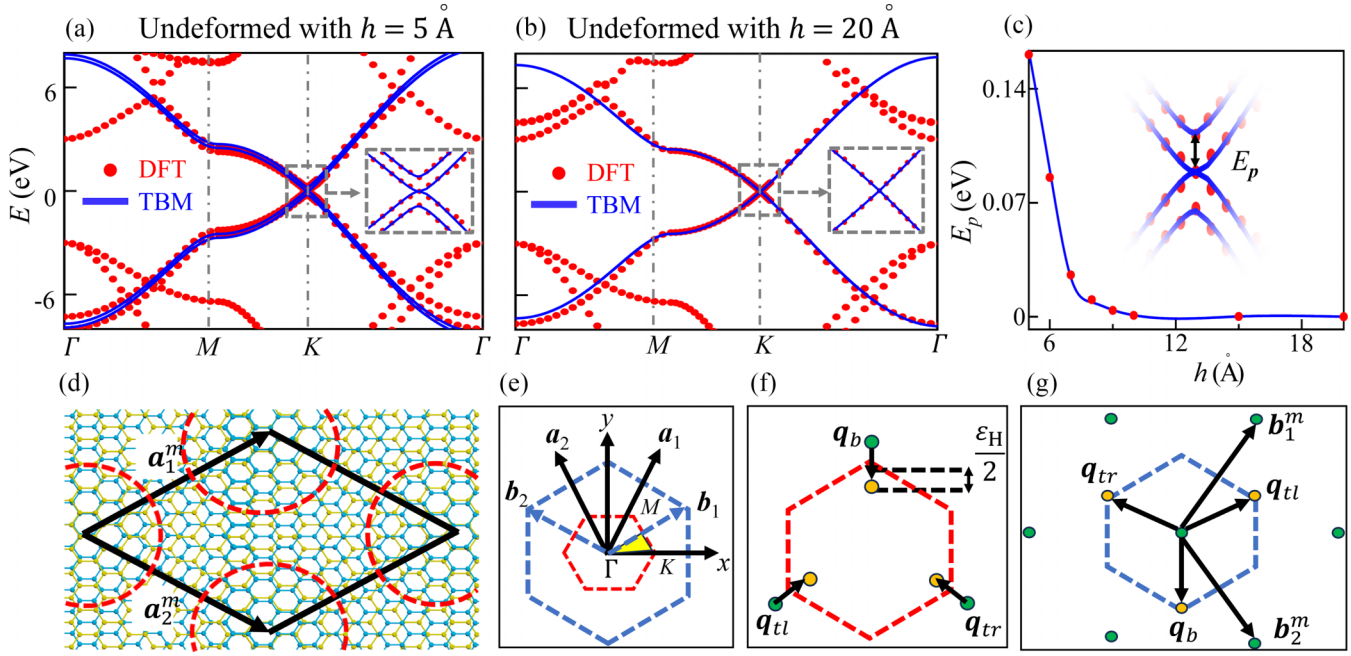

FIG. 3. Band structures for Bernal-stacked bilayer graphene with different interlayer distances: (a) $h = 5$ Å, (b) $h = 20$ Å. In (a), the inset zoom around the K point shows that the valence band and conduction band are separated from each other due to weak van der Waals forces, and in (c), such a separation is further plotted as a function of the interlayer distance h. (d) Moiré patterns in symmetrical strained bilayer graphene ($\varepsilon_H = 11.3\%$), where the red circles denote high-energy AA stacking regions and the black diamond shows the potential periodic computational domain. (e) Reciprocal lattices and (f) momentum-space diagram for the interlayer hopping for symmetrical strained bilayer graphene. The first Brillouin zone is depicted by red lines for the pristine state, and equivalent Dirac points (K and K') are marked by green (orange) dots. (g) Three distinct hopping processes in reciprocal space are depicted by $\boldsymbol{q}_b$, $\boldsymbol{q}_{tr}$, and $\boldsymbol{q}_{tl}$. The blue dashed line marks a moiré unit cell, and $\boldsymbol{b}_1^m$ and $\boldsymbol{b}_2^m$ are the basis vectors.

the increment of interlayer distance, the separation becomes smaller and tends to be negligible when the interlayer distance is larger than 10 Å. In a subsequent analysis, we consider bilayer graphene with an interlayer distance $h = 3.45$ Å, which is closer to the interlayer distance of Bernal-stacked graphene [54]. Specifically, we consider deformed bilayer graphene with one layer fixed and another layer stretched or compressed in orthogonal directions ($\varepsilon_H = 11.3\%$), as shown in Fig. 3(d). The region enclosed by black lines is the unit cell, where $\boldsymbol{a}_1^m$ and $\boldsymbol{a}_2^m$ are the basis vectors, and $\boldsymbol{q}_b$, $\boldsymbol{q}_{tr}$, and $\boldsymbol{q}_{tl}$ represent the momentum difference of the K point between the fixed layer and the biaxially stretched layer, as shown in Fig. 3(e). We consider the K points of the three nearest neighbors in the fixed layer [Fig. 3(f)], where their momentum differences to the origin exactly meet the momentum conservation law. Furthermore, the K points are staggered due to a biaxial stretch, and they constitute a new set of honeycomb lattices, thus satisfying the requirements by Eq. (6).

We compare the TBM and DFT results for bilayer graphene with biaxial symmetrical deformation ($\epsilon_x = \epsilon_y \neq 0$). As compression can easily induce wrinkling of graphene sheets in practical senses [55] and affect the electrical properties, here we only emphasize stretch conditions. An analysis on the compression conditions is available in the Supplemental Material [50]. As shown in Fig. 4(a), theoretical predictions (by TBM) are in good agreement with simulation results (by DFT), verifying the effectiveness of our TBM. Based on the established TBM, we first investigate the band structures of bilayer graphene with different stretch conditions. It is found that the curve slope near the K point decreases gradually with reduced tensile strain, which indicates a growing lower Fermi velocity. In Fig. 4(c), we show the band structure and density of states near the charge neutrality point calculated for $\varepsilon_H = 1.9\%$. A flat band is observed for the band structure and a peak value appears for the density of states at the Fermi level, which indicates that the Fermi velocity of the electron is zero, i.e., a magic strain in analogy with a magic angle is obtained. In this magic-strain case, it is difficult for the electron to hop from the conduction band to the valence band.

We adopt the McMillan formula [56] to obtain the Bardeen-Cooper-Schrieffer (BCS) superconductivity critical temperature as $T_c = \frac{\hbar\omega_D}{1.45k_B}\exp(-\frac{1.04(1+\lambda)}{\lambda-\mu_c^*(1+0.62\lambda)})$, where λ is a strong BCS coupling strength and is larger than 1, k_B is the Boltzmann constant, $\hbar\omega_D$ is the Debye frequency, and μ_c^* is the reduced Coulomb coupling strength. To reveal the dependence of T_c on the factor λ, we have to consider s-wave pairing of the bilayer graphene with symmetrical strain. In the s-wave intrasublattice channel, the local pairing amplitude is expressed as [57]

$$\Delta_l^{(s)}(\boldsymbol{r}) = \langle \Psi_{\alpha_1}(\boldsymbol{r})\Psi_{\beta_2}(\boldsymbol{r})\rangle = -\langle \Psi_{-\alpha_2}(\boldsymbol{r})\Psi_{\beta_1}(\boldsymbol{r})\rangle. \quad (8)$$

Here, α_l or β_l denote different sublattices in different layers l (1 or 2). We assume that the pair amplitude has moiré period-

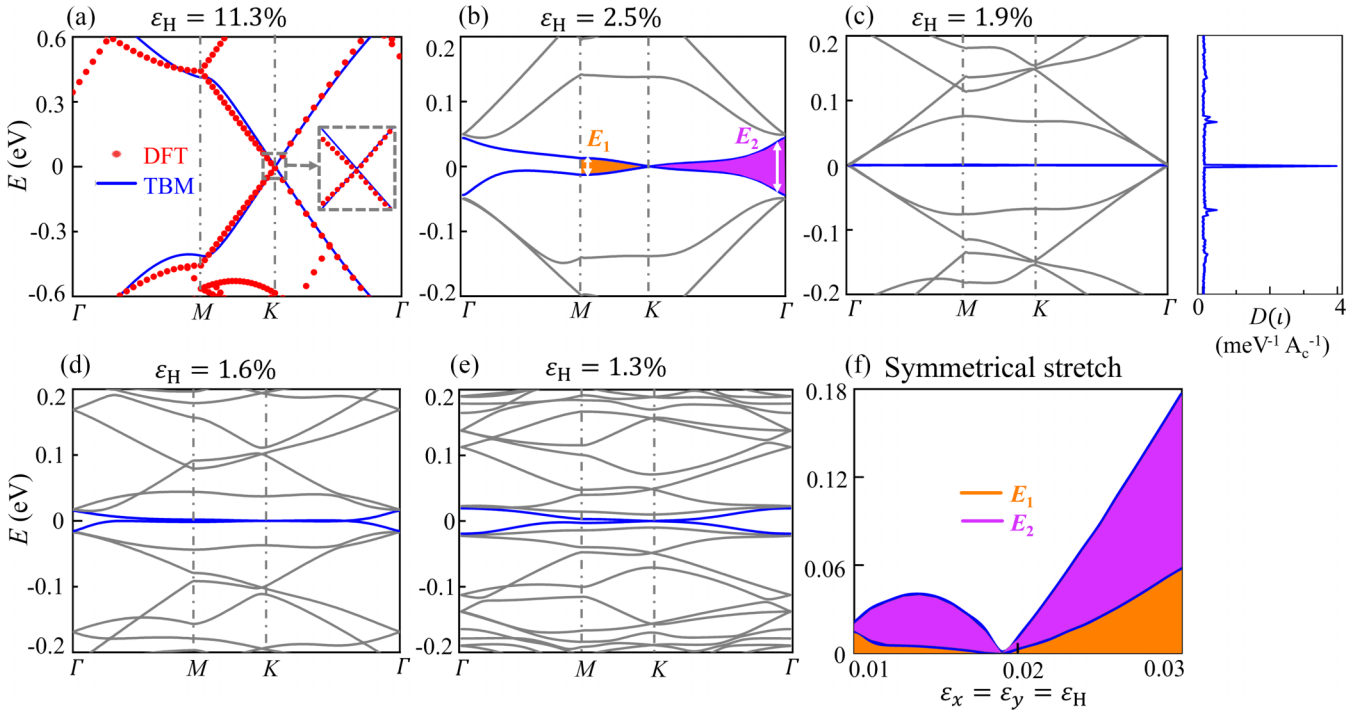

FIG. 4. Superconductivity in magic-strain bilayer graphene. Band structures of symmetrical strained bilayer graphene are shown for (a) $\varepsilon_H = 11.3\%$, (b) $\varepsilon_H = 2.5\%$, (c) $\varepsilon_H = 1.9\%$, (d) $\varepsilon_H = 1.6\%$, and (e) $\varepsilon_H = 1.3\%$. The inset zoom shows no band gap around the K point, and the Fermi velocity $V_F = 2\pi E/(\hbar k)$ decreases with inclined stretching strains, as the curve slopes around the K point decrease in the range $\varepsilon_H > 1.9\%$. For the strain condition $\varepsilon_H = 1.9\%$ in (c), a flat band is observed and a peak value appears at the Fermi level, which demonstrates potential superconductivity. E_1 and E_2 are the separation values at the M and Γ points, respectively, and they are plotted as a function of strain ε_H in (f). The band gap first gradually decays to zero at $\varepsilon_H = 1.9\%$, then increases beyond this critical value.

icity, and then we can obtain $\Delta_l^{(s)}(\boldsymbol{r}) = \sum_{\boldsymbol{b}} e^{i\boldsymbol{b}\cdot\boldsymbol{r}} \Delta_{\boldsymbol{b},l}^{(s)}$. Here, $\boldsymbol{b}$ is the moiré reciprocal lattice vector of undeformed graphene and follows

$$\Delta_{\boldsymbol{b},l}^{(s)} = \sum_{\boldsymbol{b}l} \xi_{\boldsymbol{b}_1\boldsymbol{b}_2}^{l_1 l_2} \Delta_{\boldsymbol{b},l}^{(s)},$$

$$\xi_{\boldsymbol{b}_1\boldsymbol{b}_2}^{l_1 l_2} = \frac{2g_0}{A} \sum_{\boldsymbol{q},n_1,n_2} \left(\frac{1 - n_F[\iota_{n_1}(\boldsymbol{q})] - n_F[\iota_{n_2}(\boldsymbol{q})]}{\iota_{n_1}(\boldsymbol{q}) + \iota_{n_2}(\boldsymbol{q}) - 2\mu} \times \left[\langle u_{n_1}(\boldsymbol{q}) | u_{n_2}(\boldsymbol{q})\rangle_{\boldsymbol{b}_1,l_1}\right]^* \langle u_{n_1}(\boldsymbol{q}) | u_{n_2}(\boldsymbol{q})\rangle_{\boldsymbol{b}_2,l_2} \right), \quad (9)$$

where A is the sample area, ξ is the pair susceptibility, $|u_n\rangle$ is the wave function, and g_n ($n = 0, 1, 2$) is the attractive interaction strength whose approximate value $\tilde{g}_0 = g_0 - \sqrt{3}U a_0^2/4$ is used to evaluate λ as $\lambda = \exp(\tilde{g}_0/g_0)$. Here, U is the on-site repulsion on the honeycomb lattice of each graphene layer and we have the relation $g_0 = g_1 + g_2$, where g_1 and g_2 are taken as 52 and 69 MeV nm^2, respectively [58–60]. The overlap function $\langle\cdots\rangle_{\boldsymbol{b},l}$ is the layer-resolved matrix element of the plane-wave operator $\exp(i\boldsymbol{b}\cdot\boldsymbol{r})$. Note that $\hat{\mathcal{T}}$ symmetry has been employed in Eq. (9).

The critical temperature T_c is reached when the largest eigenvalue of ξ is equal to 1. In Fig. 5, we calculate T_c for $\varepsilon_H = 1.9\%$ including $\boldsymbol{b}$ up to the third moiré reciprocal lattice vector shell. The largest value of T_c, which exceeds 10 K near the magic strain, can be understood by examining the uniform susceptibility, which has the standard form $g_0 \int d\iota D(\iota)[1 - 2n_F(\iota)]/[2(\iota - \mu)]$. Here, $D(\iota)$ is the density of states per spin valley, $n_F(\iota)$ is the Fermi-Dirac occupation function, μ is the chemical potential, and ι is the corresponding energy. Depending on the exact values of λ, the s-wave intrasublattice channel can lead to superconductivity instability. Note that we did not fulfill the tough task of exactly calculating λ and T_c for our system, but made estimations of T_c on typical λ instead. We aim to demonstrate that the high density of states at the Fermi level will induce a strong phonon-electron coupling which can cause superconductivity. Such estimations are enough for a proof-of-concept demonstration. See more details in the Supplemental Material [50]. As a quantitative illustration, we present the relationship between the band gap at Γ and M points in Fig. 4(f). It is observed that only under the magic strain $\varepsilon_H = 1.9\%$, the D value (that refers to the difference between E_1 and E_2) approaches zero, as verified by Fig. 4(c).

We further investigate the bilayer graphene system with biaxial asymmetrical strains ($\varepsilon_x \neq \varepsilon_y$). It is found that the band gaps are open only under asymmetrical strain conditions and are closed if symmetrical strains are imposed, as shown in Figs. 6(a)–6(e). The density of states is shown in the right panel of Fig. 6(c), where neither a peak value nor band gap are observed. In Fig. 6(f) we show that the band-gap value increases with an increased D value of tensile strain in the x and y directions, as a result of the increased destruction

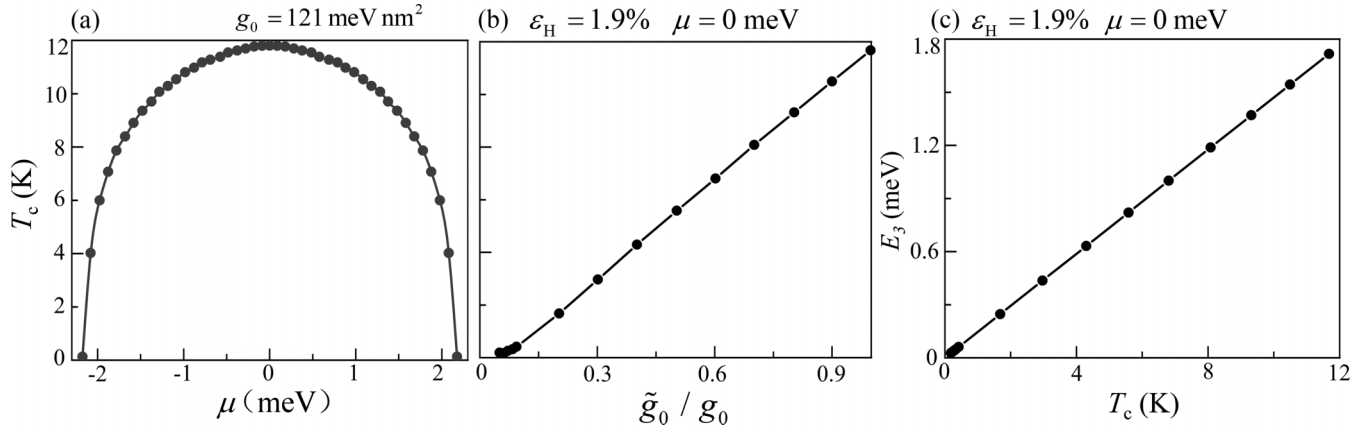

FIG. 5. Critical temperature T_c in the s wave as a function of (a) chemical potential μ and (b) reduced attractive interaction strength g_0. (c) Superconducting gap E_3 as a function of T_c. Here, $E_3 = 1.76 k_B T_c$.

of the geometrical symmetry. In the case where $\varepsilon_x = -0.15$ and $\varepsilon_y = 0.15$, the value of the band gap is observed to be 0.0272 eV, which is much smaller than its strained monolayer graphene counterpart. Such findings indicate that monolayer graphene is much easier to generate a semimetal-insulator transition than bilayer graphene when relaxation strains are imposed. In addition, the band-gap value exhibits different dependency behaviors on ε_x and ε_y, which is induced by the chiral properties of graphene.

IV. CONCLUSION

Summarizing, we have shown that relaxation-strained graphene has the potential to be a superconductor or insulator. First, asymmetrical strain distribution will result in the band-gap opening of monolayer graphene, which indicates that a semimetal-insulator transition is generated. If we impose different types of strain on monolayer graphene (compressive strain in one direction and tensile strain in another direction, $\epsilon_x \epsilon_y < 0$), the band gap will open largely due to the severe

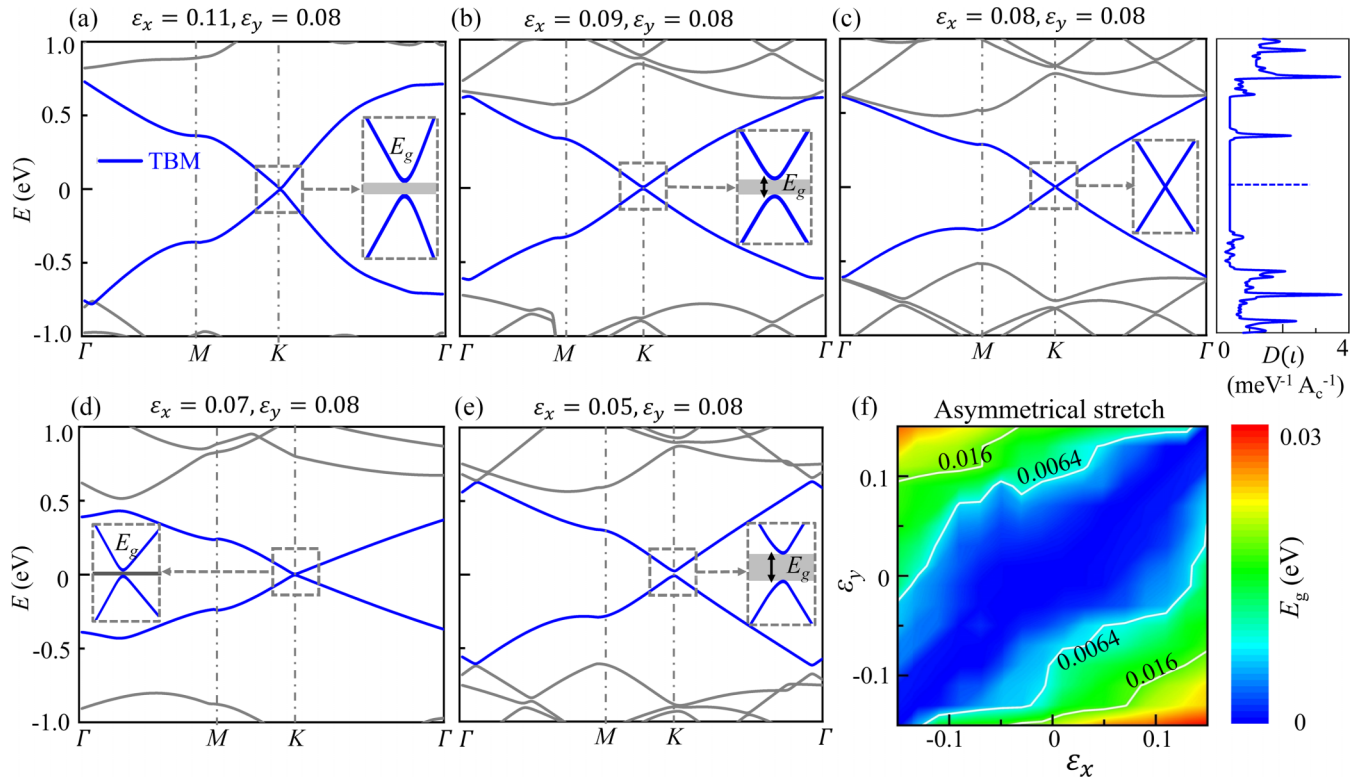

FIG. 6. Band structure for asymmetrical strained bilayer graphene: (a) $\varepsilon_x = 0.11$, (b) $\varepsilon_x = 0.09$, (c) $\varepsilon_x = 0.08$, (d) $\varepsilon_x = 0.07$, and (e) $\varepsilon_x = 0.05$, all obtained from TBM. The inset zooms around the K point show band gaps that indicate semimetal-insulator transitions. (f) Such band gaps are plotted as functions of ε_x and ε_y. The band gap increases with an increasing D value of ε_x and ε_y.

destruction of the geometrical symmetry in hexagonal lattices. By contrast, if the same types of strain are applied (compression or stretch in both directions, $\epsilon_x\epsilon_y > 0$), the band gap of monolayer graphene is small. In extreme conditions, if the stretch or compression rates in two directions are identical ($\epsilon_x = \epsilon_y$), the band gap will vanish, and also the curve slope near the K point will be reduced relative to pristine graphene, which indicates that stretch or compression will reduce the Fermi velocity. Following these findings, we compress monolayer graphene by 10% in one direction and stretch it by different rates in another direction. It is found that the band-gap value increases with the increase of strain differences. Specifically, the band gap can be as large as 0.39 eV under the condition that $\epsilon_x = -10\%$, $\epsilon_y = 20\%$. Second, a small interlayer distance will induce separation of the conduction band and valence band from each other due to weak van der Waals forces, and such a separation phenomenon can be eliminated if the interlayer distance is larger than 10 Å. Lastly, under the condition that one graphene layer is fixed while another layer is biaxially stretched (or compressed), the Fermi velocity will decrease with decreasing tensile strains. When the symmetrical strain is at the magic strain 1.9%, a flat band is generated which indicates that the bilayer graphene turns out to be a superconductor below the critical temperature. By contrast, biaxially asymmetrical stretched (or compressed) conditions will generate a band-gap opening which indicates semimetal-insulator transitions. Generally, we pave an avenue to achieve graphene superconducting or insulating states by tailoring biaxial strains. Compared with the widely used twisted systems, the relaxation strain is easier to implement in practice and adds more flexibility to obtain exotic electronic properties by strain engineering.

V. THEORY AND CALCULATION

A. Theoretical model

Considering the situation where one graphene layer is fixed and another layer is stretched in orthogonal directions, the Hamiltonian will consist of two single-layer Dirac-Hamiltonian terms and a tunneling term. In this section, we present the process to simplify the tunneling term. The matrix element for the tunneling term based on the continuum model is

$$T^{\alpha,\beta}_{\boldsymbol{k},\boldsymbol{k}'} = \langle \Psi_{\boldsymbol{k},\alpha} | H_\perp \big| \Psi^{\varepsilon}_{\boldsymbol{k}',\beta} \rangle. \tag{10}$$

Here, the tunneling Hamiltonian $H_\perp$ describes a process during which an electron with momentum $\boldsymbol{k}' = M\boldsymbol{k}$ in the fixed layer hops to the momentum state $\boldsymbol{k}$ in the stretched layer. The left and right vectors are Bloch wave functions

$$\begin{aligned} |\psi_{\boldsymbol{k},\alpha}\rangle &= \frac{1}{\sqrt{N_1N_2}} \sum_{n_1,n_2} e^{i\boldsymbol{k}\cdot(\boldsymbol{R}_{n_1,n_2}+\boldsymbol{\delta}_\alpha)} \big| \boldsymbol{R}_{n_1,n_2} + \boldsymbol{\delta}_\alpha, \alpha \big\rangle, \\ \big|\psi^{\varepsilon}_{\boldsymbol{k}',\beta}\big\rangle &= \frac{1}{\sqrt{N_1N_2}} \sum_{n_1',n_2'} e^{i\boldsymbol{k}'\cdot(\boldsymbol{R}^{\varepsilon}_{n_1',n_2'}+\boldsymbol{\delta}^{\varepsilon}_\beta)} \big| \boldsymbol{R}^{\varepsilon}_{n_1',n_2'} + \boldsymbol{\delta}^{\varepsilon}_\beta, \beta \big\rangle. \end{aligned} \tag{11}$$

where the vectors in the deformed layer have all taken into account the tensile strain, and they are set as $\alpha = A$, $\boldsymbol{\delta}_\alpha = 0$ and $\alpha = B$, $\boldsymbol{\delta}_\alpha = \boldsymbol{\delta}$. Substituting Eq. (11) into Eq. (10), we can obtain

$$\begin{aligned} T^{\alpha,\beta}_{K+\boldsymbol{q}_1,K^\varepsilon+\boldsymbol{q}_2^\varepsilon} = \frac{1}{N_1N_2} \sum_{n_1,n_2} \sum_{n_1',n_2'} & e^{-i(K+\boldsymbol{q}_1)\cdot(\boldsymbol{R}_{n_1,n_2}+\boldsymbol{\delta}_\alpha)} \\ & \times e^{i\left(K^\varepsilon+\boldsymbol{q}_2^\varepsilon\right)\cdot(\boldsymbol{R}^{\varepsilon}_{n_1',n_2'}+\boldsymbol{\delta}^{\varepsilon}_\beta)} \\ & \times \big\langle \boldsymbol{R}_{n_1,n_2} + \boldsymbol{\delta}_\alpha, \alpha \big| H_\perp \big| \boldsymbol{R}^{\varepsilon}_{n_1',n_2'} + \boldsymbol{\delta}^{\varepsilon}_\beta, \beta \big\rangle. \end{aligned}$$

We define the last term as a transition matrix element,

$$\begin{aligned} &\big\langle \boldsymbol{R}_{n_1,n_2} + \boldsymbol{\delta}_\alpha, \alpha \big| H_\perp \big| \boldsymbol{R}^{\varepsilon}_{n_1',n_2'} + \boldsymbol{\delta}^{\varepsilon}_\beta, \beta \big\rangle \\ &\quad = t_\perp\big(\boldsymbol{R}_{n_1,n_2} + \boldsymbol{\delta}_\alpha - \boldsymbol{R}^{\varepsilon}_{n_1',n_2'} - \boldsymbol{\delta}^{\varepsilon}_\beta\big), \end{aligned} \tag{12}$$

and use a Fourier transform for simplification,

$$\begin{aligned} T^{\alpha,\beta}_{K+\boldsymbol{q}_1,K^\varepsilon+\boldsymbol{q}_2^\varepsilon} = \frac{1}{(N_1N_2)^2} \sum_{n_1,n_2} \sum_{n_1',n_2'} \sum_{\boldsymbol{k}} & e^{i[\boldsymbol{k}-(K+\boldsymbol{q}_1)]\cdot\boldsymbol{R}_{n_1,n_2}} \\ & \times e^{i[(K^\varepsilon+\boldsymbol{q}_2^\varepsilon)-\boldsymbol{k}]\cdot\boldsymbol{R}^{\varepsilon}_{n_1',n_2'}} \\ & \times e^{i[\boldsymbol{k}-(K+\boldsymbol{q}_1)]\cdot\boldsymbol{\delta}_\alpha + \boldsymbol{\tau}\times e^{i[(K^\varepsilon+\boldsymbol{q}_2^\varepsilon)-\boldsymbol{k}]\cdot(\boldsymbol{\delta}^{\varepsilon}_\beta-\boldsymbol{\delta}+\boldsymbol{\tau})\frac{t_\perp(K)}{A_{\text{u.c.}}}}}. \end{aligned} \tag{13}$$

We then define reciprocal lattice vectors to simplify Eq. (13), and transform its form from real space to reciprocal space:

$$\begin{aligned} T^{\alpha,\beta}_{K+\boldsymbol{q}_1,K^\varepsilon+\boldsymbol{q}_2^\varepsilon} = \sum_{k,l,m,n} & \frac{t_\perp(K+\boldsymbol{q}_1+\boldsymbol{G}_{k,l})}{A_{\text{u.c.}}} \\ & \times e^{i[\boldsymbol{G}_{k,l}\cdot\boldsymbol{\delta}_\alpha - \boldsymbol{G}_{m,n}\cdot(\boldsymbol{\delta}^{\varepsilon}_\beta-\boldsymbol{\delta}) - \boldsymbol{G}^{\varepsilon}_{m,n}\cdot\boldsymbol{\tau}]} \\ & \times \delta_{K+\boldsymbol{q}_1+\boldsymbol{G}_{k,l},K^\varepsilon+\boldsymbol{q}_2^\varepsilon+\boldsymbol{G}^{\varepsilon}_{m,n}}. \end{aligned} \tag{14}$$

Here, $\boldsymbol{G}$ is summed over reciprocal lattice vectors. The main contribution sum in the formula $T^{\alpha,\beta}_{K+\boldsymbol{q}_1,K^\varepsilon+\boldsymbol{q}_2^\varepsilon}$ originates from $\boldsymbol{G}_{m,n}$, $\boldsymbol{b}_2^\varepsilon$, and $-\boldsymbol{b}_1^\varepsilon$, hence $K + \boldsymbol{G}^{\varepsilon}_{m,n}$ correspond to three K points. In this manner, $\boldsymbol{q}_1$ and $\boldsymbol{q}_2^\varepsilon$, which are close to K and K^ε, can satisfy the momentum conservation law. Substituting the value $\boldsymbol{G}_{m,n}$ into the above equations, we then obtain

$$\begin{aligned} T^{\alpha,\beta}_{K+\boldsymbol{q}_1,K^\varepsilon+\boldsymbol{q}_2^\varepsilon} = \frac{t_\perp(K)}{A_{\text{u.c.}}} \big[& \delta_{K+\boldsymbol{q}_1,K^\varepsilon+\boldsymbol{q}_2^\varepsilon} + e^{i[\boldsymbol{b}_2\cdot(\boldsymbol{\delta}_\alpha-\boldsymbol{\delta}^{\varepsilon}_\beta+\boldsymbol{\delta})-\boldsymbol{b}_2^\varepsilon\cdot\boldsymbol{\tau}]} \\ & \times \delta_{K+\boldsymbol{q}_1+\boldsymbol{b}_2,K^\varepsilon+\boldsymbol{q}_2^\varepsilon+\boldsymbol{b}_2^\varepsilon} \\ & + e^{-i[\boldsymbol{b}_1\cdot(\boldsymbol{\delta}_\alpha-\boldsymbol{\delta}^{\varepsilon}_\beta+\boldsymbol{\delta})-\boldsymbol{b}_1^\varepsilon\cdot\boldsymbol{\tau}]} \delta_{K+\boldsymbol{q}_1-\boldsymbol{b}_1,K^\varepsilon+\boldsymbol{q}_2^\varepsilon-\boldsymbol{b}_1^\varepsilon} \big]. \end{aligned} \tag{15}$$

Here, all four possible degrees of freedom for the sublattice are $\{\alpha, \beta\} = \{A, B\}$, $\boldsymbol{\delta}_A = 0$, $\boldsymbol{\delta}_B = \boldsymbol{\delta}$. Then we can write the transition matrix in a two-order form,

$$T = \begin{bmatrix} T^{A,A} & T^{A,B} \\ T^{B,A} & T^{B,B} \end{bmatrix}. \tag{16}$$

Thus we can obtain the simplified tunneling term that describes interlayer hopping as

$$T^{\alpha,\beta}_{K+\boldsymbol{q}_1,K^\varepsilon+\boldsymbol{q}_2^\varepsilon} = T_{\boldsymbol{q}_b}\delta_{\boldsymbol{q}_2^\varepsilon-\boldsymbol{q}_1,\boldsymbol{q}_b} + T_{\boldsymbol{q}_{tr}}\delta_{\boldsymbol{q}_2^\varepsilon-\boldsymbol{q}_1,\boldsymbol{q}_{tr}} + T_{\boldsymbol{q}_{tl}}\delta_{\boldsymbol{q}_2^\varepsilon-\boldsymbol{q}_1,\boldsymbol{q}_{tl}}, \tag{17}$$

where $\boldsymbol{\delta}$ is a vector connecting the two atoms in the unit cell, and α and β are the sublattice numbers for the fixed layer and stretched layer, respectively. The transition matrices are given by

$$T_{\boldsymbol{q}_b} = \frac{t_\perp(K)}{A_{\text{u.c.}}} \begin{bmatrix} 1 & 1 \\ 1 & 1 \end{bmatrix},$$

$$T_{q_{tr}} = \frac{t_\perp(K)}{A_{\text{u.c.}}} e^{-\boldsymbol{b}_2^m \cdot \boldsymbol{\tau}} \begin{bmatrix} e^{-i\theta} & 1 \\ e^{i\theta} & e^{-i\theta} \end{bmatrix},$$

$$T_{q_{tl}} = \frac{t_\perp(K)}{A_{\text{u.c.}}} e^{-\boldsymbol{b}_1^m \cdot \boldsymbol{\tau}} \begin{bmatrix} e^{i\theta} & 1 \\ e^{-i\theta} & e^{i\theta} \end{bmatrix},$$

where $\boldsymbol{\tau}$ is a translation vector that is almost zero for a small stretch factor, and $\boldsymbol{b}_1^m$ and $\boldsymbol{b}_2^m$ are basis vectors for reciprocal lattices shown in Fig. 3(e). Details on the establishing process of the TBM for different graphene systems are provided in the Supplemental Material [50].

B. Density functional theory calculation

All DFT calculations are conducted using the Vienna *ab initio* simulation package (VASP). The generalized gradient approximation (GGA) and Perdew-Burke-Ernzerhof (PBE) function are employed for the exchange-correlation functions. Additionally, the projector augmented-wave (PAW) method is utilized to describe the electron interactions. The van der Waals interactions are accounted for using the DFT-D2 method. The truncation energy of plane waves is set to be 550 eV. Structural optimization is considered complete when the force on each atom is less than 0.01 eV/Å. During the process of structural relaxation, a $5 \times 5 \times 1$ K-point mesh, based on the Monkhorst-Pack scheme, is employed for geometrical optimization. Similarly, a $15 \times 15 \times 1$ K-point mesh is used for electronic structure calculations. Different K-point paths are selected based on the specific graphene models under investigation [50].

ACKNOWLEDGMENTS

This work was supported by the National Natural Science Foundation of China (Grants No. 12302169 and No. 12172102); by the European Union, under Marie Skłodowska-Curie Actions Postdoctoral Fellowships (No. 101149710); and by the French Investissements d'Avenir program, in part by the ANR PNanoBot (ANR-21-CE33-0015) and ANR OPTOBOTS project (ANR-21-CE33-0003). Computations have been performed on the supercomputer facilities of the Mésocentre de calcul de Franche-Comté.

Q.J. and M.K. conceptualized the formal analysis; B.L. and J.C. were in charge of the methodology; J.C. was in charge of software, data curation, and investigation; C.W. and M.K. supervised and validated the work; C.W. was the project administrator; Q.J. wrote the original draft; J.C. and M.K. reviewed and edited the work.

The authors declare that they have no known competing financial interests or personal relationships that could have appeared to influence the work reported in this paper.

DATA AVAILABILITY

The data supporting this study's findings are available within the article.

[1] J. Christensen, A. I. Fernandez-Dominguez, F. de Leon-Perez, L. Martin-Moreno, and F. Garcia-Vidal, Collimation of sound assisted by acoustic surface waves, Nat. Phys. **3**, 851 (2007).

[2] K. Yu, N. X. Fang, G. Huang, and Q. Wang, Magnetoactive acoustic metamaterials, Adv. Mater. **30**, 1706348 (2018).

[3] N. Jiménez, W. Huang, V. Romero García, V. Pagneux, and J. P. Groby, Ultra-thin metamaterial for perfect and quasi-omnidirectional sound absorption, Appl. Phys. Lett. **109**, 121902 (2016).

[4] R. Schittny, M. Kadic, T. Bückmann, and M. Wegener, Invisibility cloaking in a diffusive light scattering medium, Science **345**, 427 (2014).

[5] Z. Wang, Q. Zhang, K. Zhang, and G. Hu, Tunable digital metamaterial for broadband vibration isolation at low frequency, Adv. Mater. **28**, 9857 (2016).

[6] R. Schittny, M. Kadic, S. Guenneau, and M. Wegener, Experiments on transformation thermodynamics: Molding the flow of heat, Phys. Rev. Lett. **110**, 195901 (2013).

[7] Z. Ding, X. Li, Q. Ji, Y. Zhang, H. Li, H. Zhang, L. Pattelli, Y. Li, H. Xu, and J. Zhao, Machine-learning-assisted design of a robust biomimetic radiative cooling metamaterial, ACS Mater. Lett. **6**, 2416 (2024).

[8] J. K. Gansel, M. Thiel, M. S. Rill, M. Decker, K. Bade, V. Saile, G. von Freymann, S. Linden, and M. Wegener, Gold helix photonic metamaterial as broadband circular polarizer, Science **325**, 1513 (2009).

[9] M. Amin, O. Siddiqui, H. Abutarboush, M. Farhat, and R. Ramzan, A THz graphene metasurface for polarization selective virus sensing, Carbon **176**, 580 (2021).

[10] M. Kadic, G. W. Milton, M. van Hecke, and M. Wegener, 3D metamaterials, Nat. Rev. Phys. **1**, 198 (2019).

[11] D. R. Smith, J. B. Pendry, and M. C. Wiltshire, Metamaterials and negative refractive index, Science **305**, 788 (2004).

[12] D. Schurig, J. J. Mock, B. Justice, S. A. Cummer, J. B. Pendry, A. F. Starr, and D. R. Smith, Metamaterial electromagnetic cloak at microwave frequencies, Science **314**, 977 (2006).

[13] A. K. Geim and I. V. Grigorieva, Van der Waals heterostructures, Nature (London) **499**, 419 (2013).

[14] K. S. Novoselov, A. Mishchenko, A. Carvalho, and A. Castro Neto, 2D materials and van der Waals heterostructures, Science **353**, aac9439 (2016).

[15] Y. Meng, J. Feng, S. Han, Z. Xu, W. Mao, T. Zhang, J. S. Kim, I. Roh, Y. Zhao, D.-H. Kim *et al.*, Photonic van der Waals integration from 2D materials to 3D nanomembranes, Nat. Rev. Mater. **8**, 498 (2023).

[16] T. Zhao, P. Xie, H. Wan, T. Ding, M. Liu, J. Xie, E. Li, X. Chen, T. Wang, Q. Zhang *et al.*, Ultrathin MXene assemblies approach the intrinsic absorption limit in the 0.5–10 THz band, Nat. Photonics **17**, 622 (2023).

[17] J. Qin, M. Wang, and C. W. Qiu, Graphene metasurface hits the point, Light: Sci. Appl. **12**, 110 (2023).

[18] J. Christensen, A. Manjavacas, S. Thongrattanasiri, F. H. Koppens, and F. J. García de Abajo, Graphene plasmon waveguiding and hybridization in individual and paired nanoribbons, ACS Nano **6**, 431 (2012).

[19] L. Ponomarenko, R. Gorbachev, G. Yu, D. Elias, R. Jalil, A. Patel, A. Mishchenko, A. Mayorov, C. Woods, J. Wallbank

et al., Cloning of Dirac fermions in graphene superlattices, Nature (London) **497**, 594 (2013).

[20] P. San-Jose, J. González, and F. Guinea, Non-Abelian gauge potentials in graphene bilayers, Phys. Rev. Lett. **108**, 216802 (2012).

[21] S. Ichinokura, K. Sugawara, A. Takayama, T. Takahashi, and S. Hasegawa, Superconducting calcium-intercalated bilayer graphene, ACS Nano **10**, 2761 (2016).

[22] F. Massee, Y. Huang, M. Golden, and M. Aprili, Noisy defects in the high-T_c superconductor $Bi_2Sr_2CaCu_2O_{8+x}$, Nat. Commun. **10**, 544 (2019).

[23] Y. Liu, T. Wei, G. He, Y. Zhang, Z. Wang, and J. Wang, Pair density wave state in a monolayer high-T_c iron-based superconductor, Nature (London) **618**, 934 (2023).

[24] K. H. Jin, H. Huang, J. Mei, Z. Liu, L. K. Lim, and F. Liu, Topological superconducting phase in high-T_c superconductor MgB_2 with Dirac–nodal-line fermions, npj Comput. Mater. **5**, 57 (2019).

[25] F. Guinea, M. I. Katsnelson, and A. Geim, Energy gaps and a zero-field quantum Hall effect in graphene by strain engineering, Nat. Phys. **6**, 30 (2010).

[26] N. N. Klimov, S. Jung, S. Zhu, T. Li, C. A. Wright, S. D. Solares, D. B. Newell, N. B. Zhitenev, and J. A. Stroscio, Electromechanical properties of graphene drumheads, Science **336**, 1557 (2012).

[27] J. Lu, A. C. Neto, and K. P. Loh, Transforming moiré blisters into geometric graphene nano-bubbles, Nat. Commun. **3**, 823 (2012).

[28] J. Zabel, R. R. Nair, A. Ott, T. Georgiou, A. K. Geim, K. S. Novoselov, and C. Casiraghi, Raman spectroscopy of graphene and bilayer under biaxial strain: bubbles and balloons, Nano Lett. **12**, 617 (2012).

[29] B. Amorim, A. Cortijo, F. De Juan, A. G. Grushin, F. Guinea, A. Gutiérrez-Rubio, H. Ochoa, V. Parente, R. Roldán, P. San-Jose *et al.*, Novel effects of strains in graphene and other two dimensional materials, Phys. Rep. **617**, 1 (2016).

[30] J. Mao, S. P. Milovanović, M. Anelković, X. Lai, Y. Cao, K. Watanabe, T. Taniguchi, L. Covaci, F. M. Peeters, A. K. Geim *et al.*, Evidence of flat bands and correlated states in buckled graphene superlattices, Nature (London) **584**, 215 (2020).

[31] Z. Li, Y. Lv, L. Ren, J. Li, L. Kong, Y. Zeng, Q. Tao, R. Wu, H. Ma, B. Zhao *et al.*, Efficient strain modulation of 2D materials via polymer encapsulation, Nat. Commun. **11**, 1151 (2020).

[32] S. Yang, Y. Chen, and C. Jiang, Strain engineering of two-dimensional materials: Methods, properties, and applications, InfoMat **3**, 397 (2021).

[33] M. T. Mahmud, D. Zhai, and N. Sandler, Topological flat bands in strained graphene: Substrate engineering and optical control, Nano Lett. **23**, 7725 (2023).

[34] Y. Cao, V. Fatemi, S. Fang, K. Watanabe, T. Taniguchi, E. Kaxiras, and P. Jarillo-Herrero, Unconventional superconductivity in magic-angle graphene superlattices, Nature (London) **556**, 43 (2018).

[35] R. Bistritzer and A. H. MacDonald, Moiré bands in twisted double-layer graphene, Proc. Natl. Acad. Sci. USA **108**, 12233 (2011).

[36] G. Tarnopolsky, A. J. Kruchkov, and A. Vishwanath, Origin of magic angles in twisted bilayer graphene, Phys. Rev. Lett. **122**, 106405 (2019).

[37] C. Chen, W. Tang, X. Chen, Z. Kang, S. Ding, K. Scott, S. Wang, Z. Li, J. P. Ruff, M. Hashimoto *et al.*, Anomalous excitonic phase diagram in band-gap-tuned $Ta_2Ni(Se,S)_5$, Nat. Commun. **14**, 7512 (2023).

[38] G. Hu, Q. Ou, G. Si, Y. Wu, J. Wu, Z. Dai, A. Krasnok, Y. Mazor, Q. Zhang, Q. Bao *et al.*, Topological polaritons and photonic magic angles in twisted α-MoO_3 bilayers, Nature (London) **582**, 209 (2020).

[39] L. A. Gonzalez-Arraga, J. L. Lado, F. Guinea, and P. San-Jose, Electrically controllable magnetism in twisted bilayer graphene, Phys. Rev. Lett. **119**, 107201 (2017).

[40] J. M. Park, Y. Cao, K. Watanabe, T. Taniguchi, and P. Jarillo-Herrero, Tunable strongly coupled superconductivity in magic-angle twisted trilayer graphene, Nature (London) **590**, 249 (2021).

[41] Q. Ji, Z. Xue, Z. Zhang, Z. Cui, M. Kadic, and C. Wang, Interlayer torsional sliding and strain localization in bilayer graphene, Proc. R. Soc. A **479**, 20220833 (2023).

[42] V. Morovati, Z. Xue, K. M. Liechti, and R. Huang, Interlayer coupling and strain localization in small-twist-angle graphene flakes, Extreme Mech. Lett. **55**, 101829 (2022).

[43] R. Banerjee, V.-H. Nguyen, T. Granzier-Nakajima, L. Pabbi, A. Lherbier, A. R. Binion, J.-C. Charlier, M. Terrones, and E. W. Hudson, Strain modulated superlattices in graphene, Nano Lett. **20**, 3113 (2020).

[44] B. S. Jessen, L. Gammelgaard, M. R. Thomsen, D. M. Mackenzie, J. D. Thomsen, J. M. Caridad, E. Duegaard, K. Watanabe, T. Taniguchi, T. J. Booth *et al.*, Lithographic band structure engineering of graphene, Nat. Nanotechnol. **14**, 340 (2019).

[45] F. Guinea and N. R. Walet, Electrostatic effects, band distortions, and superconductivity in twisted graphene bilayers, Proc. Natl. Acad. Sci. USA **115**, 13174 (2018).

[46] N. Nakatsuji and M. Koshino, Moiré disorder effect in twisted bilayer graphene, Phys. Rev. B **105**, 245408 (2022).

[47] Z. Zhang, L. Wen, Y. Qiao, and Z. Li, Effects of strain on the flat band in twisted bilayer graphene, Chin. Phys. B **32**, 107302 (2023).

[48] J. H. Wong, B. R. Wu, and M. F. Lin, Strain effect on the electronic properties of single layer and bilayer graphene, J. Phys. Chem. C **116**, 8271 (2012).

[49] G. Catarina, B. Amorim, E. V. Castro, J. Lopes, and N. Peres, Twisted bilayer graphene: Low-energy physics, electronic and optical properties, in *Handbook of Graphene*, edited by E. Celasco *et al.* (Wiley, Hoboken, NJ, 2019), Chap. 6, pp. 177–231.

[50] See Supplemental Material at http://link.aps.org/supplemental/10.1103/5v5w-8vtn for the tight-binding model and charge density of strained graphene, which includes Refs. [51,52].

[51] A. V. Rozhkov, A. Sboychakov, A. Rakhmanov, and F. Nori, Electronic properties of graphene-based bilayer systems, Phys. Rep. **648**, 1 (2016).

[52] S. Das Sarma and E. H. Hwang, Collective modes of the massless Dirac plasma, Phys. Rev. Lett. **102**, 206412 (2009).

[53] M. Van der Donck, F. M. Peeters, and B. Van Duppen, Transport properties of bilayer graphene in a strong in-plane magnetic field, Phys. Rev. B **93**, 115423 (2016).

[54] X. Chang, Y. Ge, and J. Dong, Ripples of *AA* and *AB* stacking bilayer graphenes, Eur. Phys. J. B **78**, 103 (2010).

[55] C. Androulidakis, E. Koukaras, M. P. Carbone, M. Hadjinicolaou, and C. Galiotis, Wrinkling formation in simply-supported graphenes under tension and compression loadings, Nanoscale **9**, 18180 (2017).

[56] W. McMillan, Transition temperature of strong-coupled superconductors, Phys. Rev. **167**, 331 (1968).

[57] F. Wu, A. H. MacDonald, and I. Martin, Theory of phonon-mediated superconductivity in twisted bilayer graphene, Phys. Rev. Lett. **121**, 257001 (2018).

[58] R. Ribeiro, V. M. Pereira, N. Peres, P. Briddon, and A. C. Neto, Strained graphene: Tight-binding and density functional calculations, New J. Phys. **11**, 115002 (2009).

[59] B. Roy, J. D. Sau, and S. Das Sarma, Migdal's theorem and electron-phonon vertex corrections in dirac materials, Phys. Rev. B **89**, 165119 (2014).

[60] T. O. Wehling, E. Şaşıoğlu, C. Friedrich, A. I. Lichtenstein, M. I. Katsnelson, and S. Blügel, Strength of effective Coulomb interactions in graphene and graphite, Phys. Rev. Lett. **106**, 236805 (2011).